Bayesian environmental inversion of airgun modal dispersion using a single hydrophone in the Chukchi Sea

Graham A. Warner,[a] Stan E. Dosso, and Jan Dettmer
School of Earth and Ocean Sciences, University of Victoria, 3800 Finnerty Road, Suite A405, Victoria, British Columbia V8P 5C2, Canada

David E. Hannay
JASCO Applied Sciences, 2305-4464 Markham Street, Victoria, British Columbia V8Z 7X8, Canada

(Received 24 November 2014; revised 11 February 2015; accepted 3 May 2015)

This paper presents estimated water-column and seabed parameters and uncertainties for a shallow-water site in the Chukchi Sea, Alaska, from trans-dimensional Bayesian inversion of the dispersion of water-column acoustic modes. Pulse waveforms were recorded at a single ocean-bottom hydrophone from a small, ship-towed airgun array during a seismic survey. A warping dispersion time-frequency analysis is used to extract relative mode arrival times as a function of frequency for source-receiver ranges of 3 and 4 km which are inverted for the water sound-speed profile (SSP) and subbottom geoacoustic properties. The SSP is modeled using an unknown number of sound-speed/depth nodes. The subbottom is modeled using an unknown number of homogeneous layers with unknown thickness, sound speed, and density, overlying a halfspace. A reversible-jump Markov-chain Monte Carlo algorithm samples the model parameterization in terms of the number of water-column nodes and subbottom interfaces that can be resolved by the data. The estimated SSP agrees well with a measured profile, and seafloor sound speed is consistent with an independent headwave arrival-time analysis. Environmental properties are required to model sound propagation in the Chukchi Sea for estimating sound exposure levels and environmental research associated with marine mammal localization.
 [http://dx.doi.org/10.1121/1.4921284]

[ZHM] Pages: 3009–3023

I. INTRODUCTION

Knowledge of ocean sound-speed profiles (SSP) and seabed geoacoustic properties is required for the accurate prediction of underwater sound propagation, such as used for marine mammal noise impact assessments and for sonar-performance studies. For long-range propagation in shallow water, the geoacoustic properties are particularly important because of numerous interactions with the bottom. Low frequencies are more sensitive to deep subbottom structure and large-scale SSP features. High frequencies do not penetrate the subbottom as deeply but are more sensitive to finer-scale SSP features. These environmental dependencies mean measurements of broadband sound contain substantial information about the environment.

In range-independent shallow-water environments, long-range sound propagation is well modeled with normal-mode theory.[1] The environment acts as a dispersive waveguide which supports a limited number of propagating modes, with the modal group speeds directly dependent on the environment. The frequency-dependence of mode arrival times (i.e., modal dispersion) can be used as data in an environmental inversion if the source-receiver range is known. Dispersion measurements can be made using a single hydrophone; however, resolving mode arrival times in the time-frequency (TF) plane is dependent on the difference in modal group speeds, source-receiver range, and the signal processing techniques applied. At long ranges, modes are well separated in time and arrival times can be determined from a spectrogram; however, there is more opportunity for environmental range-dependence to affect arrival times. Also, higher attenuation for higher-order modes degrades environmental information contained in long-range data. Short-range measurements are less susceptible to range-dependent effects and have higher bandwidth but TF resolution limitations can degrade estimates of mode arrival times. Recent studies have used mode-warping techniques to improve the TF resolution of modal arrival times for close-range dispersion measurements[2–6] and this approach is used here. Fourier series or variations thereof[7] are then used for the TF representations but the inherent side lobes (leakage) from Fourier transforms means that correlated errors can exist between arrival times for adjacent frequencies. These correlations should be taken into account in an inversion algorithm.

Environmental inversion of modal dispersion data has been carried out for several types of impulsive sources.[2,3,6–10] These studies have either used prior knowledge or the Bayesian information criterion (BIC) to determine the subbottom layering parameterization (i.e., the number of layers). Parameterization is important because having too few layers under-parameterizes the model and under-fits

[a]Present address: JASCO Applied Sciences, 2305-4464 Markham Street, Victoria, British Columbia V8Z 7X8, Canada. Electronic mail: gwarner@uvic.ca

the data, potentially leaving structure unresolved and under-estimating uncertainties. Conversely, too many layers over-parameterizes the model and overfits data, allowing spurious unconstrained structure and over-estimating uncertainties. Prior knowledge of the layering structure (e.g., from a core or high-resolution seismic survey), even if accurate, may not be appropriate if the resolution of the dispersion data is not consistent with that of the prior information. The BIC estimates the most appropriate parameterization (given strong assumptions), but because it is a point estimate, parameter uncertainties may be underestimated. This paper uses a trans-dimensional[11–14] (trans-D) Bayesian inversion approach for subbottom layering that allows the information content of the data to determine how much subbottom structure can be resolved. The trans-D algorithm samples probabalistically over possible parameterizations, and model parameter uncertainties include the uncertainty in parameterization. The geoacoustic model consists of an unknown number of homogeneous layers defined by interface depths, sound speeds, and densities overlying a halfspace.

The same concerns for parameterization apply to the SSP. Several studies have inverted for the SSP using empirical orthogonal functions calculated from existing SSP measurements for the location.[8,9] This method simplifies the inversion in that only a small number (e.g., 2 or 3) coefficients of SSP eigenfunctions are inverted for instead of the sound speed at a series of depths; however, the eigenfunctions must be calculated from a comprehensive SSP data base which may not be available for all environments. Another approach is to assume a fixed number of nodes defining the SSP but this requires *a priori* knowledge of an appropriate number of nodes which may not be available. Given the above limitations, an alternative and more general approach to estimating the SSP is developed for this study. The SSP is modeled in terms of a set of depth/sound-speed nodes, with the profile interpolated from these nodes as $1/c_w^2$ linear gradients (c_w is water sound speed). The number of nodes is sampled probabilistically with a trans-D algorithm so the data estimate how much SSP structure can be resolved. The node at the base of the SSP determines the water depth and sound speed at the seafloor, coupling the two trans-D stacks (SSP and subbottom). To our knowledge, trans-D inversion has not been previously applied to modal dispersion inversion.

Previous Bayesian modal-dispersion work[6] has taken error correlations into account using a fixed (point) estimate of the data covariance matrix from residual analysis. However, for trans-D models this assumes that the parameterization used for the point estimate is representative for the trans-D posterior which is difficult to assess and may not be sufficient for measured data. In this paper, we use a trans-D first-order auto-regressive [AR(1)] error model to account for potential residual error correlations.[15]

The Bayesian approach applied here quantifies model parameter uncertainties and the trans-D formulation for the SSP and geoacoustic profile accounts for the uncertainty in the environmental parameterization. The trans-D auto-regressive error model accounts for residual error correlations without overparameterizing the error model when correlations are weak or absent. This approach reduces subjective choices in determining appropriate model parameterizations.

The trans-D Bayesian inversion is applied to acoustic data collected using autonomous ocean-bottom hydrophone (OBH) recorders that were part of an underwater sound measurement program in the Chukchi Sea, approximately 140 km offshore the northwest coast of Alaska.[16] The program was originally designed to determine distances to specific sound level thresholds from an airgun array used in seismic surveys to assess shallow hazards to drilling operations (e.g., near-surface gas) by Shell Oil Company. In addition to fulfilling the program objectives, the acoustic recordings of airgun pulses were found to be well suited for environmental inversion. This location is of significant interest because of potential hydrocarbon deposits and the presence of large numbers of marine mammals (e.g., bowhead whales, beluga, walrus, and several species of seals are commonly observed here). To our knowledge, there are no published geoacoustic properties to sufficient depth to accurately model low-frequency sound propagation at this location (surficial sediments are a mixture of sand, silt, and clay[17,18] but sediment properties can change dramatically with depth). One of the goals of this paper is therefore to estimate site-specific environmental properties that can be used in future work to predict sound propagation for estimating sound exposure levels as a function of range and for marine-mammal localization to help understand animal behavior and mitigate anthropogenic effects on the animals.

II. THEORY

A. Data processing

Small synchronously fired airgun arrays produce low-frequency (below ~500 Hz) impulsive sounds of durations short enough that all frequencies can be modeled as being emitted at the same instant for the purposes of analyzing dispersion measurements. The propagation of airgun pulses can be modeled using normal-mode theory.[1] Modes propagate with different group speeds that are dependent on the environment, i.e., water-column SSP and geoacoustic properties of the subbottom. The group speeds can be calculated using a normal-mode model.[19] The arrival time of mode m at frequency f for pulse p at a recorder at range r is

$$t_{mp}(f) = \tau_p + \frac{r_p}{v_m(f)}, \tag{1}$$

where τ_p is the pulse time and $v_m(f)$ is the group speed. For this paper, we analyze multiple pulses where the inter-pulse distance is fixed and known, i.e., $r_{p+1} - r_p = \Delta r \ \ \forall p$.

The modal arrival times as a function of frequency can be determined from the TF representations of a pulse recorded at a single hydrophone. Previous studies have used a mode warping technique to improve the modal TF resolution from impulsive sources such as imploding light bulbs or explosive charges measured at close range.[2–6] Mode warping is a nonlinear resampling technique that transforms dispersive modes into constant-frequency tones. A band-pass filter

can then be used to isolate individual modes and the filtered signal transformed back into the time domain.

A signal $p(t)$ is transformed to the warped time domain as

$$q(w) = \sqrt{|w'(t)|}\, p[w(t)], \tag{2}$$

where $w(t)$ is the warping function with time derivative $w'(t)$ and $q(w)$ is the warped signal. The warped signal can be unwarped by using Eq. (2) with $w^{-1}(t)$ as the warping function and $q(w)$ as the signal. For an isospeed waveguide with rigid bottom and free surface, the warping function for dispersive modes is[20]

$$w(t) = \sqrt{t^2 + (r/c_w)^2}, \tag{3}$$

where r is the range and c_w is the water sound speed. This warping function was found suitable for low-frequency modes in several shallow-water environments despite violations of the ideal waveguide assumption.[2–6] A suitable value for the ratio r/c_w can be determined empirically by observing when modes become constant-frequency tones in a spectrogram of q. The warped pulse is filtered for each of M modes and unwarped, resulting in M mono-component signals $p_m(t)$. Figure 1 illustrates this procedure for the recording of an airgun pulse at 4 km range (described in Sec. V).

For each filtered mode, a spectrogram is computed using a Hanning window with 99% overlap (Fig. 1 considers a 8192-point window for data sampled at 48 kHz). The mode arrival times are set to the time of maximum energy at each frequency. The bandwidth of each mode is limited by the environment in terms of the mode cutoff at low frequencies and modal attenuation at high frequencies. Near modal cutoff, the dispersion curves tail back around the slower airy phase but the spectrogram resolution for these rapid TF changes is poor. In addition, the modal amplitude changes rapidly near the cutoff frequency which can bias the arrival-time estimate. Lower-frequency data are therefore limited to frequencies above the inflection point of the time vs frequency curve. Modes at high frequencies arrive closely spaced in time due to their more similar modal group speeds. The spectrogram is not good at resolving such signals, so the modes are truncated if the arrival time for successive frequencies fall into the same time window.

B. Bayesian Inversion

The picks of arrival time vs frequency indicated on Figs. 1(d)–1(g) represent acoustic data which can be inverted for environmental parameters. The inversion carried out in this paper uses a trans-D Bayesian formulation[21,22] which is

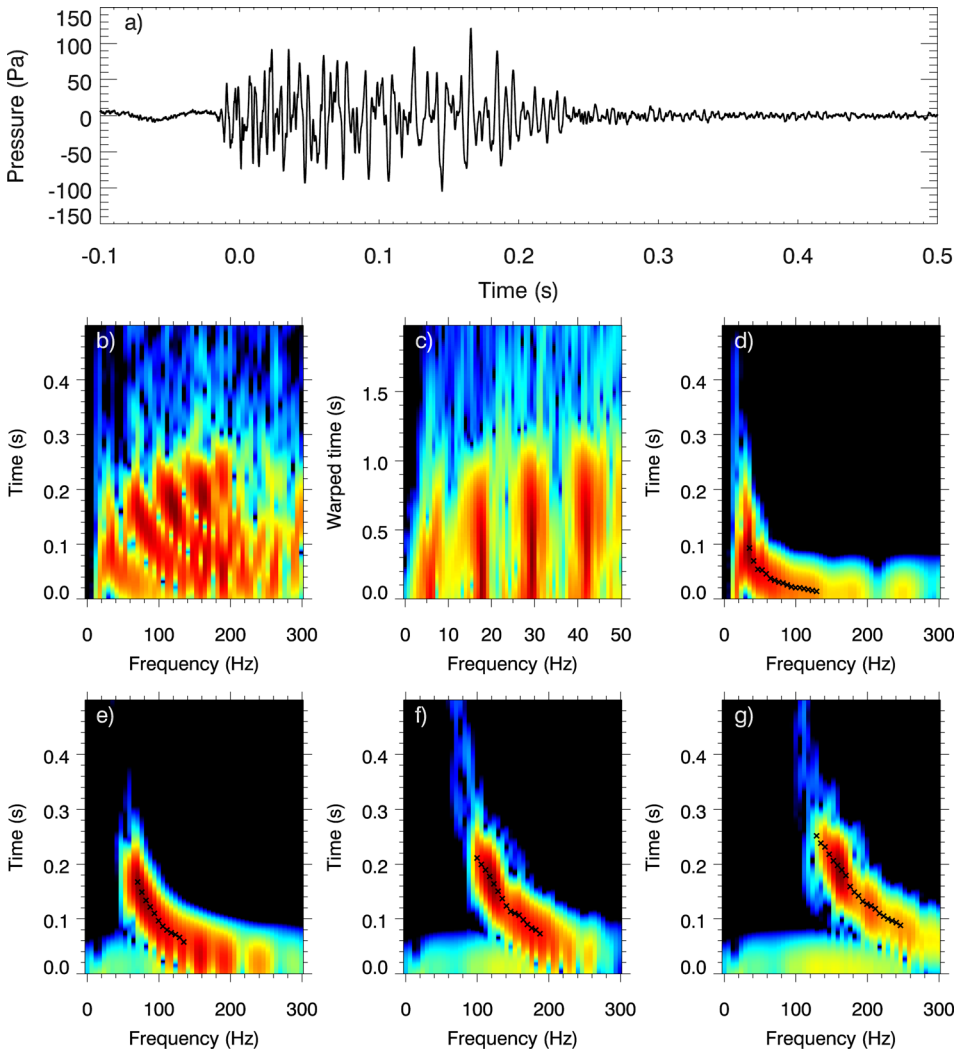

FIG. 1. (Color online) Example of warping TF analysis. (a) Measured airgun pulse waveform at 4 km range. (b) Unfiltered spectrogram. (c) Warped spectrogram showing four warped modes as approximate constant-frequency tones. (d)–(g) Filtered spectrograms with data picks (×) for modes 1–4, respectively. Note that higher-order modes are resolved to higher frequency than possible in the unfiltered spectrogram.

briefly described here; a more detailed formulation is provided in the Appendix. The environmental model consists of a water column with unknown depth and SSP over a seabed consisting of an unknown number of homogeneous fluid layers (each layer characterized by thickness, sound speed, and density) overlying a fluid halfspace of unknown geoacoustic parameters. Mode group speeds are calculated for an environmental model using the normal-mode code ORCA[19] and are converted to predicted modal arrival times using pulse time and range [Eq. (1)]. In a Bayesian formulation the solution is given by properties of the posterior probability density (PPD) of the model parameters given the measured data and prior information. A reversible-jump Markov-chain Monte Carlo algorithm is applied to sample the PPD over a trans-D model space in which the number of SSP nodes and seabed layers can change by probabilistically accepting transitions between model parameters/parameterizations according to the Metropolis-Hastings-Green criterion.[12] Model transitions to higher dimensions (increased number of nodes or layers) are proposed from the prior rather than restricted to small perturbations to the current model to increase transition acceptance rate.[22] The transition acceptance probability depends on the prior, proposal, and likelihood ratios, with the likelihood defined by the assumption of Gaussian-distributed errors with unknown standard deviation and a trans-D autoregressive process to represent possible error correlations[15] over frequency for each mode of each pulse (see the Appendix). Uniform prior bounds are used for all model parameters, with an additional joint prior that constrains subbottom sound speed and density to physically realistic combinations.[23,24] The Markov-chain samples over the number and parameters of SSP nodes, subbottom layers, and autoregressive coefficients to estimate the trans-D PPD.

III. SIMULATION STUDY

This section illustrates and verifies the data analysis and inversion methodologies in a realistic simulation study. The environmental model for the simulation has five subbottom interfaces and four water-column SSP nodes. The true parameter values and the bounds of the uniform prior distributions assumed for all parameters are listed in Table I, and the joint prior distribution for subbottom sound speed and density is described in the Appendix. Mode arrival times (the observed synthetic data) were generated in two ways to produce two simulated datasets to compare inversion results. First, data were simulated using Eq. (1) with exact modal group speeds calculated by the normal-mode code ORCA,[19] i.e., we bypassed the TF data-processing step of identifying mode arrival times (Sec. II A). Gaussian-distributed errors were added to the synthetic data with standard deviations that were constant over frequency but varied between modes and between pulses from 2 to 4 ms, as given in Table II. The second dataset was created to represent a more realistic simulation that requires TF analysis to identify mode arrival times. Synthetic acoustic waveforms (time series) were modeled using Fourier synthesis of frequency-domain responses computed using ORCA from 5 to 500 Hz with 1-Hz frequency spacing. Two waveforms (A and B) for receivers at 3- and 4-km range at 3 m above the seafloor were computed assuming an impulse source function at time $\tau = 0$ and 2-m source depth. Mode arrival times were determined as described in Sec. II A for five modes in each pulse and were limited to an upper frequency bound of 300 Hz. Random errors were not added to the picked data so the inversion results illustrate uncertainties resulting only from data processing limitations, which we believe are a major component of the errors for measured data. In practice, ambient noise may also contaminate mode arrivals; however, mode arrivals that have low signal-to-noise ratios can be discarded from the inversion during data processing. We refer to the first and second datasets as the Gaussian and picked datasets, respectively. For comparison with the Gaussian dataset error statistics, residuals were computed from the difference between the exact (theoretical, noise-free) times and the picked dataset. The resulting standard deviations are listed for each pulse and mode in Table II. The Gaussian dataset was limited to the same modes and frequencies that were resolved using the data processing method on the picked dataset so the data information content is similar between datasets.

Inversions were performed on the two synthetic datasets with approximately 600 000 samples drawn from the PPD via the trans-D Bayesian inversion described in Sec. II and the Appendix. Fixed-length chain thinning[25] (described in Appendix Sec. 1) restricted the number of samples that were saved to 250 000, and saved samples that survived the fixed-length thinning process from the first 100 000 samples were

TABLE I. Model parameter values and prior bounds for the simulations. Note that subbottom sound speed and density were further constrained by the joint prior bound (see Appendix Sec. 3).

Parameter	Unit	True value(s)	Prior
c_w at surface	m/s	1447	[1439,1455]
c_w at seafloor	m/s	1440	[1439,1455]
Water depth z_b	m	41	[38,45]
Number of SSP nodes	—	4	[0,15]
SSP node depths	m	[12.85,15,24,31]	[0,z_b]
SSP node $\mathbf{c}_w$	m/s	[1447,1442,1453,1440]	[1439,1455]
Number of subbottom interfaces	—	5	[0,10]
Interface depths	m	[2,5,10,20,40]	[0,50]
Layer speed $\mathbf{c}_b$	m/s	[1465,1555,1605,1730,2200]	[1460,2500]
Basement c_b	m/s	2300	[1460,2500]
Layer density $\boldsymbol{\rho}$	g/cm^3	[1.49,1.77,1.87,2.06,2.2]	[1.3,2.5]
Basement ρ	g/cm^3	2.3	[1.3,2.5]
Pulse A range	m	3000	[2950,3050]
Pulse A time	s	0	[−1, 1]
Pulse B time	s	0	[−1, 1]

TABLE II. Error and residual standard deviations for the simulation with Gaussian (σ_G) and picked (σ_p) datasets, respectively.

Pulse	1	1	1	1	1	2	2	2	2	2
Mode	1	2	3	4	5	1	2	3	4	5
σ_G (ms)	2.0	3.0	4.0	4.0	4.0	2.0	3.0	4.0	4.0	4.0
σ_p (ms)	3.0	3.2	4.1	4.3	5.6	2.1	3.2	4.0	1.9	4.8

discarded as burn-in. Both inversions produced approximately Gaussian-distributed data residuals (not shown). Figure 2 shows the resulting marginal probability profiles for the SSP and geoacoustic parameters for the two datasets. These profiles are normalized independently at each depth to more clearly illustrate the range of values, and the corresponding probability ratio profiles to the right of the marginal profiles indicate the relative scaling. This figure also shows the marginal profiles for the SSP-node and subbottom-interface depths. The SSP distributions near the bottom of the water column are not smooth because the water-depth distributions (discussed below) constrain the available depths of SSP nodes. The estimated SSP for the Gaussian dataset is in excellent agreement with the true profile (dashed line) with reasonably small uncertainties. For the picked dataset, the estimated SSP agrees closely with the true profile between 10- and 35-m depth. The speeds near the surface and bottom are somewhat overestimated; these discrepancies are discussed later in this section.

The geoacoustic probability profiles agree well with the larger scale features of the true profile, although some small-scale features (e.g., layers as thin as 2 m) cannot be resolved by the data and are averaged in the inversion results. For the Gaussian dataset, the inversion resolves two layers above a halfspace and effectively averages the properties of the first three layers. Three layers are resolved above a halfspace for

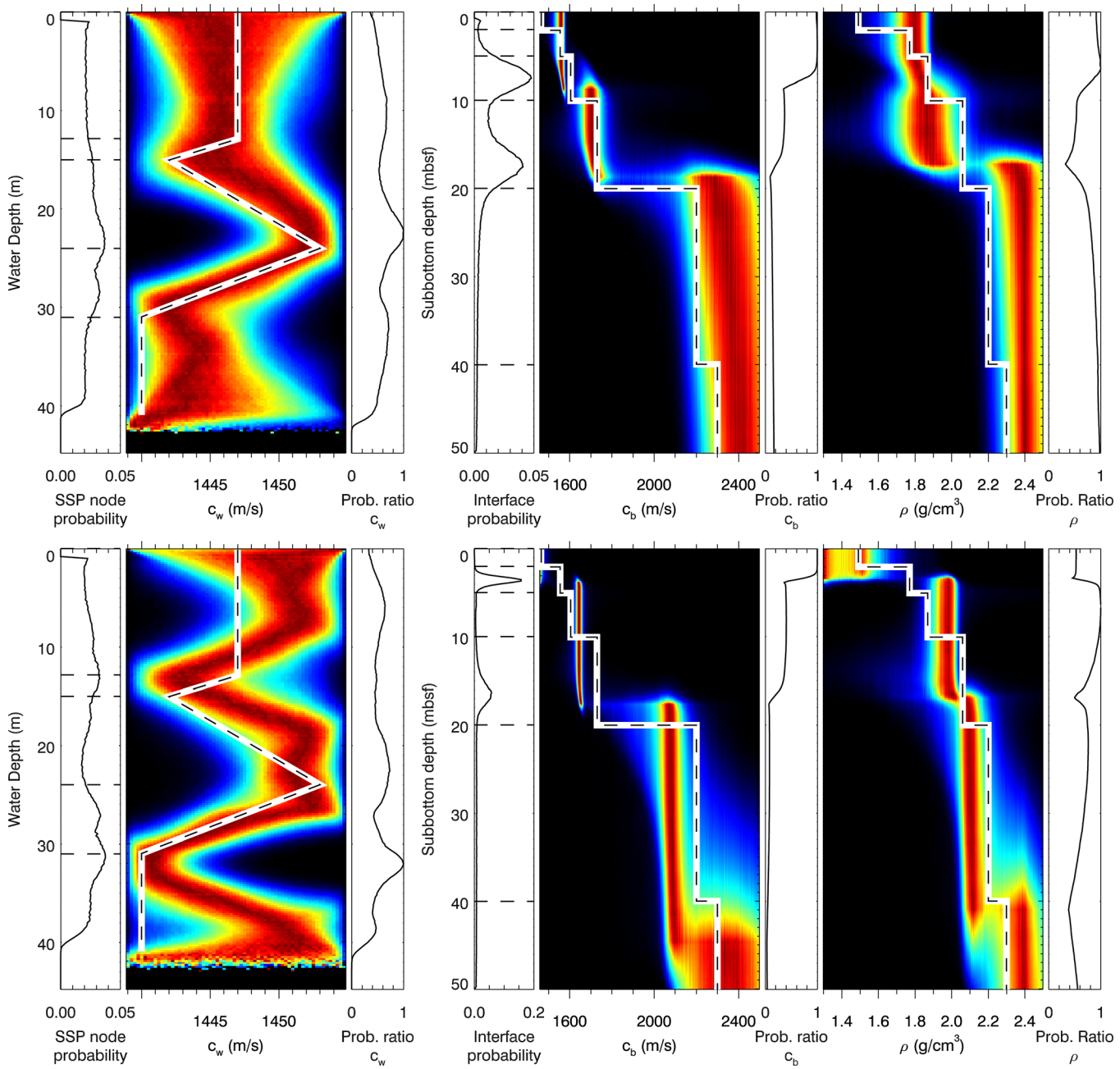

FIG. 2. (Color online) Marginal probability profiles for water SSP and bottom sound speed and density, together with their corresponding node/interface depth profiles and depth normalization profiles. Top and bottom panels show results from inverting exact dispersion calculations with additive Gaussian noise and from data picked from synthetic waveforms (but no additive noise), respectively. Plot bounds are the prior bounds for SSP and geoacoustic parameters, though subbottom sound speed and density are further constrained by a joint prior distribution (see the Appendix). True parameter values are shown with dashed lines.

the picked dataset. The shallowest layer is estimated to be somewhat too thick, and the three deeper layers are effectively averaged. The uncertainty in the profiles increases with depth and around layer interfaces for each dataset. The increase in uncertainty with depth is due to the mode functions decaying exponentially into the seabed which decreases the data sensitivity to deeper structure (considered further in Sec. V).

The inversion of the Gaussian dataset accurately resolved the environmental profiles and did not introduce any spurious structure. Discrepancies between the true and estimated profiles are due to the noise (Gaussian errors) and the limited resolution of the data. For the picked dataset, the inversion has higher subbottom resolution but introduces spurious SSP structure near the seafloor. We attribute the SSP discrepancies to errors resulting from the inherent limitations of the data processing method. Such errors may not occur for all modal dispersion data, but these discrepancies indicate the possibility even when residuals appear Gaussian distributed. Since data processing is required in all practical cases, for the remainder of this section, we only consider the picked dataset results.

Figure 3 shows the marginal distributions of the number of subbottom interfaces and SSP nodes sampled in the inversion. The most-probable number of interfaces is three, which again indicates that the data cannot resolve all five interfaces. The most-probable number of SSP nodes is six which overestimates the true number of nodes (4) and may be related to the spurious SSP structure in Fig. 2 (bottom).

Figure 4 shows the marginal probability densities for pulse times, ranges, and water depth (note that pulse B range is not an estimated parameter as it is fixed at 1 km larger than pulse A range for the simulation). The marginal distribution for pulse A range is essentially flat within the prior bounds indicating the data are not able to constrain this parameter. The pulse times are constrained well within their prior bounds of [−1, 1] s. The joint marginal distribution between pulse A range and time indicates these parameters are strongly (negatively) correlated. Hence, the prior bounds on source range play an important role in constraining source times. The

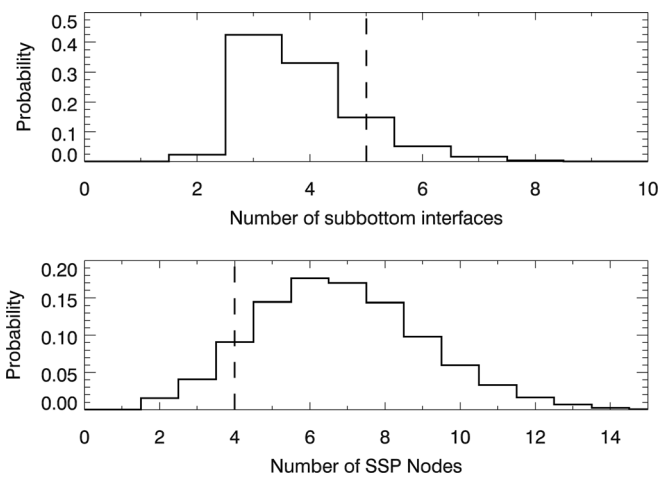

FIG. 3. Probability distributions for the (top) number of subbottom interfaces and (bottom) SSP nodes for the picked-data simulation. True values are shown with dashed lines.

absolute value of the reciprocal slope of the joint distribution, approximately 1409 m/s, represents the average modal group speed weighted by the mode standard deviations. The water depth is resolved well within the prior bounds, restricting the SSP node depth distribution and decreasing the SSP probability ratio near the seafloor (Fig. 2).

The fit to the data achieved in the inversion is shown in Fig. 5. The relative arrival times from the mode-filtered spectrograms (picked data) are shown with × symbols; marginal densities of the relative predicted arrival times, calculated from a random sample of 5000 models from the PPD, are shown as grey-scale bars (sometimes quite thin vertically), and the (error-free) theoretical relative arrival times calculated from Eq. (1) are shown with solid lines. Each marginal density is normalized individually for display purposes. The inversion sampled models that produce predicted times in excellent agreement with the picked times (i.e., the data that were inverted) but have worse agreement with the theoretical (true) times due to some correlated errors between the picked and theoretical times from data processing (e.g., mode 5). Figure 6 shows the error statistics for each mode and pulse, i.e., the marginal densities of the residual standard deviations, the fraction of time for which the AR process was required, and the marginal distributions of the AR parameters when the AR process was required. The peaks of the residual standard-deviation densities are generally slightly less than the standard deviations between exact and picked data given in Table II. The inversion required the AR process to be in effect for 30%–70% of the samples, depending on the mode. These results show that the data processing method can result in errors which have both correlated and uncorrelated components.

IV. CHUKCHI SEA SURVEY

Underwater recordings of airgun array pulses were collected 16 August 2009 during a seismic survey in the Chukchi Sea, AK, designed to assess shallow hazards for seabed drilling.[16] The recordings were made using two ocean-bottom hydrophone (OBH) recorders sampling at 48 kHz, each equipped with two hydrophones: Reson TC4043 (nominal sensitivity −201 dB re 1 V/μPa) and Reson TC4032 (nominal sensitivity −166 dB re 1 V/μPa). The OBHs were deployed 200 and 1000 m off a survey line from the survey vessel *RV Mt. Mitchell*, and the deployment locations of the OBHs were recorded using a handheld global positioning system (GPS) at 71°17.439′N, 163°38.115′W and 71°17.470′N, 163°39.436′W, with water depth measured using the ship's onboard echosounder at approximately 41 m. The bottom at this site is known to be very flat with seafloor slope on the order of 0.01%.

The source array consisted of four 10 in.^{3} airguns arranged in a 1-m long by 0.6-m wide rectangle which was towed at 2-m depth approximately 47 m behind the *RV Mt. Mitchell*. The airguns were fired synchronously every 15 m along a 25-km survey line. Airgun pulses were measured at ranges from 200 m to 20 km as the source was towed past the recorders. The *RV Mt. Mitchell* logged its coordinates every second along the survey line, which were then translated into

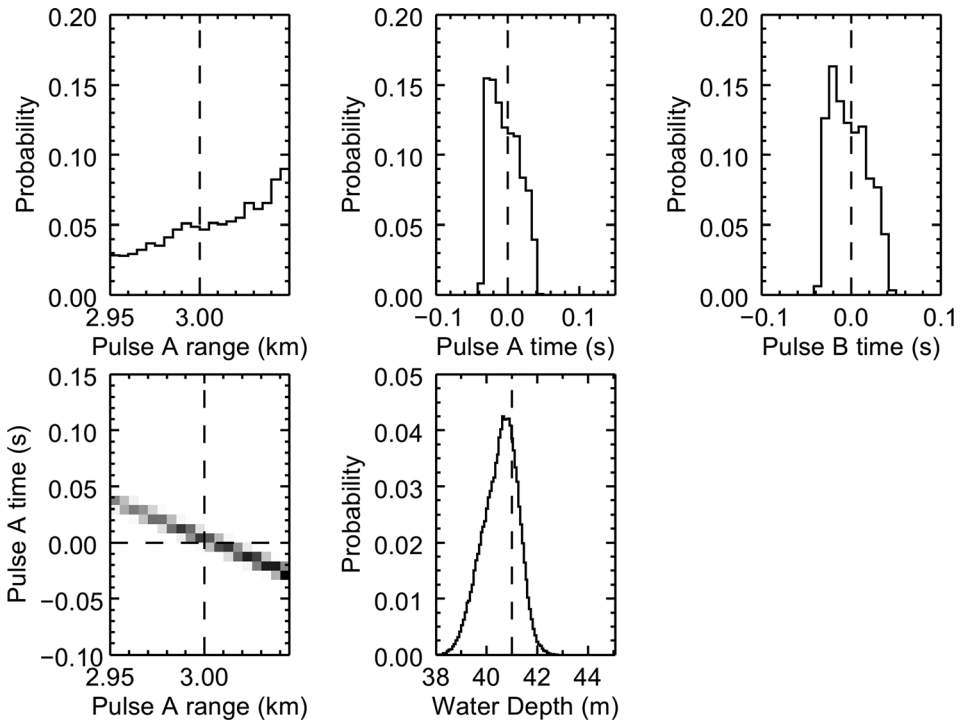

FIG. 4. Marginal probability densities for pulse range, time, and water depth for the picked-data simulation. True values are shown with dashed lines. Pulse time axes are restricted within their prior distributions; all other axes ranges indicate prior bounds.

source coordinates of the airgun array by shifting the ship track by the tow distance.

The data used for the inversion were from pulses emitted south of the OBHs recorded on the more sensitive hydrophone of the 200-m offset recorder. Two pulses, A and B, spaced 66 pulses apart (i.e., $\Delta r = 15\,\text{m} \times 66 = 990\,\text{m}$) were used for the inversion. The range for pulse A was 2978 m according to GPS records, but to account for uncertainty in the OBH deployment position and airgun coordinates, this range is treated as an unknown parameter in the inversion with prior bounds ± 50 m from the estimated range. Knowing the 990-m pulse spacing between pulses A and B, the range for pulse B was set for each model based on the range for pulse A. These pulses were selected because the ranges are long enough that modal dispersion is easily measured, but not so long that higher-order modes are strongly attenuated or that potential environmental range-dependent

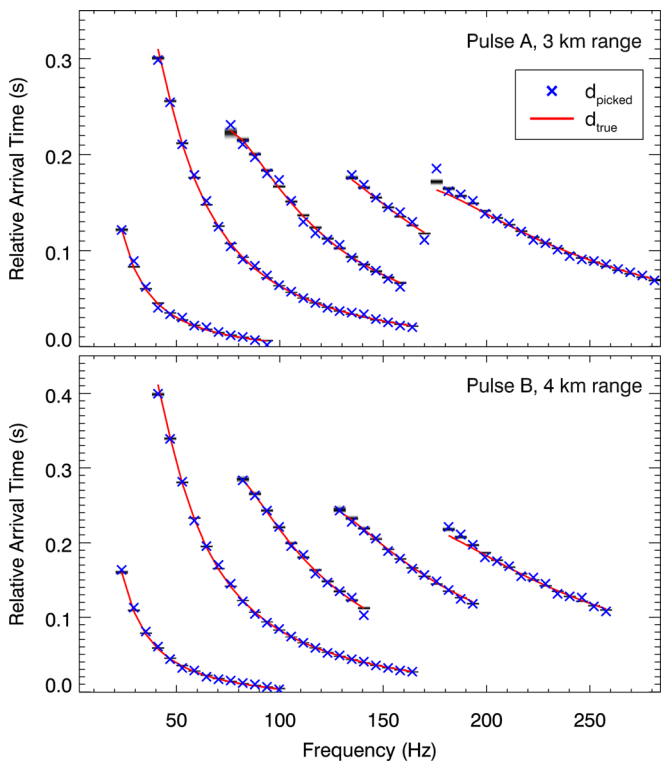

FIG. 5. (Color online) Mode relative arrival times for the two simulated pulses calculated from a random sample of models from the PPD (grey-scale distributions sometimes quite thin), the arrival times picked from the synthetic pulses (×), and the true (error-free) arrival times (solid lines).

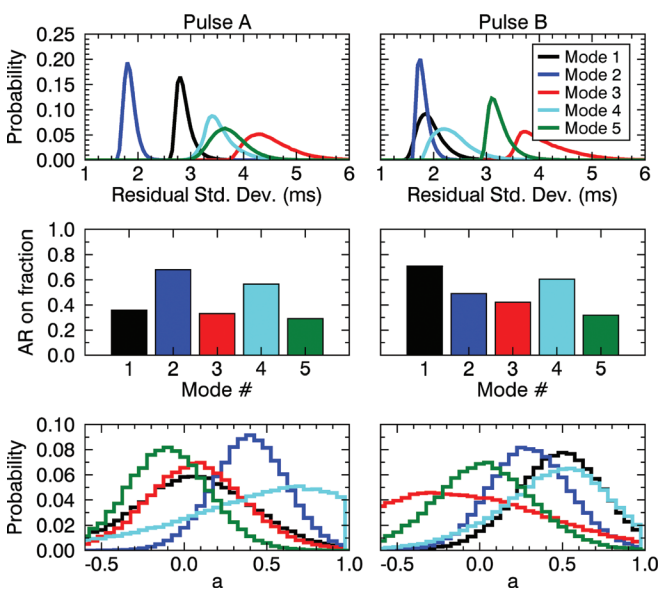

FIG. 6. Error statistics for modes in simulated (left) pulse A and (right) pulse B. Residual standard deviations, fraction of time the AR process was required (or "on"), and AR coefficient values are shown in the top, middle, and bottom panels, respectively.

effects accumulate and violate the range-independent assumption. Accurate pulse times τ_s are not known because OBH clock drift desynchronized the pulse logs with the acoustic recordings. Pulse times are therefore treated as inversion parameters with prior bounds [−3, 0] and [−4, 0] s for pulses A and B, respectively, to allow physically realistic pulse times. Prior bounds other than for range and time are identical to those in Table I. Relative arrival times were picked as described in Sec. II A for 5 and 4 modes in pulses A and B, respectively. Modes were required to have arrival times for at least ten frequencies to estimate meaningful residual error statistics (see the Appendix). Within hours of the acoustic measurements, a conductivity-temperature-depth (CTD) cast was conducted 5.7 km north of the recorder site. Since the water-column conditions are expected to be quite stable in this region, the SSP calculated from the CTD cast provides reasonable "ground-truth" to compare with the SSP inversion results.

V. RESULTS

The trans-D Bayesian inversion was applied to the measured data in a manner similar to that described for the simulation study with approximately the same number of models sampled from the PPD. Figure 7 shows the marginal profile densities for the SSP and geoacoustic parameters. Similar to the simulation study, the SSP distribution near the seafloor is not smooth because the water depth distribution constrains the available depths of SSP nodes. The measured SSP (solid line overtop the corresponding distribution) shows a well-mixed (iso-speed) surface layer from 0 to 12 m and a second slower mixed-layer from 30 to 40 m, reaching the seafloor. Between these layers, the high sound speed from 17 to 30 m is likely due to a warm-water intrusion from the Bearing Sea, which is a common feature of the Chukchi Sea in August.[26] The SSP inversion result is in excellent agreement with the measured profile, closely tracking the depth-dependent structure with reasonably small uncertainties. Although the SSP marginal profile clearly resolves the structure of the measured SSP, the node-depth distribution is relatively uninformative. The marginal profiles for subbottom sound speed and density indicate well-resolved, near-constant values for an upper sediment layer which has relatively low density for its sound speed, although these parameter values are consistent with empirical studies.[23] The most probable interface depth is 14.6 mbsf, below which there is little resolved structure. The 95% credibility interval for interface depth is [11.6, 19.2] mbsf for single-interface models (credibility interval for interface depth for all models does not accurately quantify the dominant interface depth uncertainty because the distribution has heavy tails from other interfaces). The halfspace sound speed and density are not well constrained by the data.

Figure 8 shows the marginal distributions for the number of subbottom interfaces and SSP nodes. The most probable number of subbottom interfaces is one, supporting a single subbottom layer over a halfspace model. The most probable number of SSP nodes is six but the distribution is wider than for seabed interfaces.

Figure 9 shows the marginal probability densities for pulse times, range, and water depth. Similar to the simulation study, the marginal distribution for pulse-A range is essentially the prior distribution. Pulse times are constrained well within their prior bounds. The slope of the joint distribution between pulse-A range and time corresponds to an average modal group speed of approximately 1428 m/s. The 95% credibility interval for water depth is [41.6, 43.3] m. The water depth at the OBH deployment site was measured

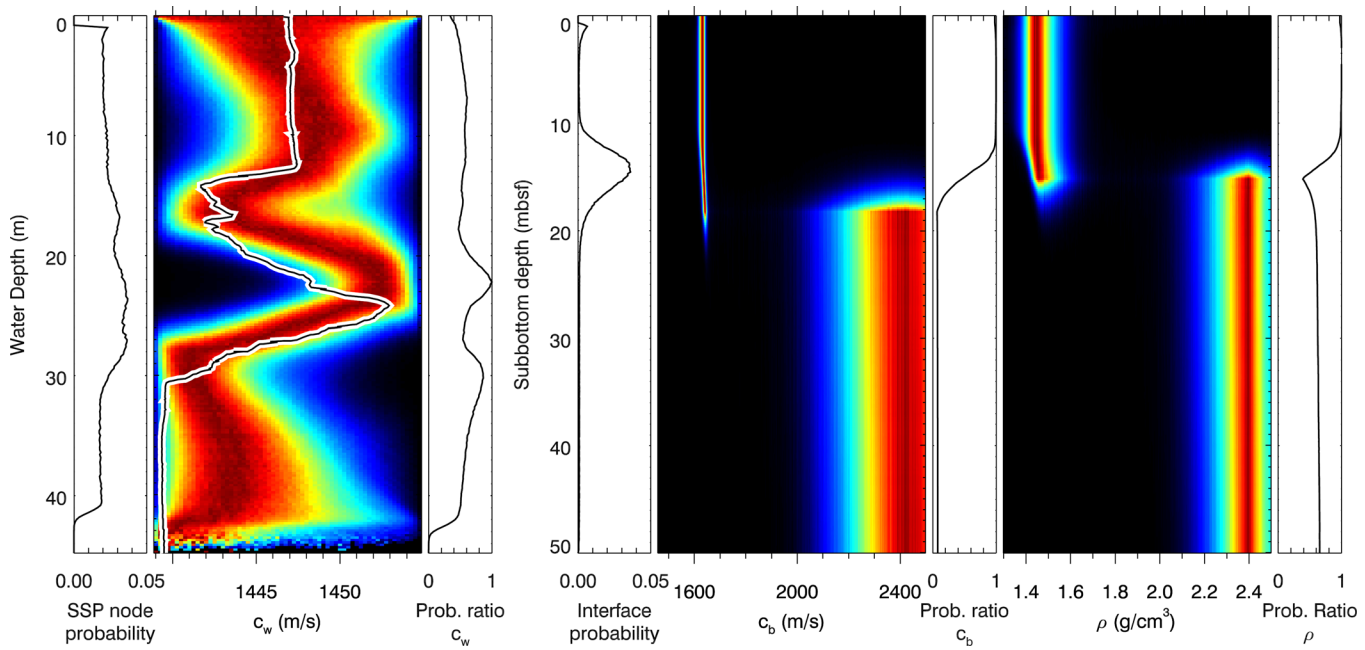

FIG. 7. (Color online) Marginal probability profiles for water SSP and bottom sound speed and density, together with their corresponding node/interface depth profiles and depth normalization profiles. The solid line in the second panel shows the SSP measured 5.7 km from the OBH. Plot bounds are the prior bounds for SSP and geoacoustic parameters, though subbottom sound speed and density have been further constrained by a joint prior distribution (see the Appendix).

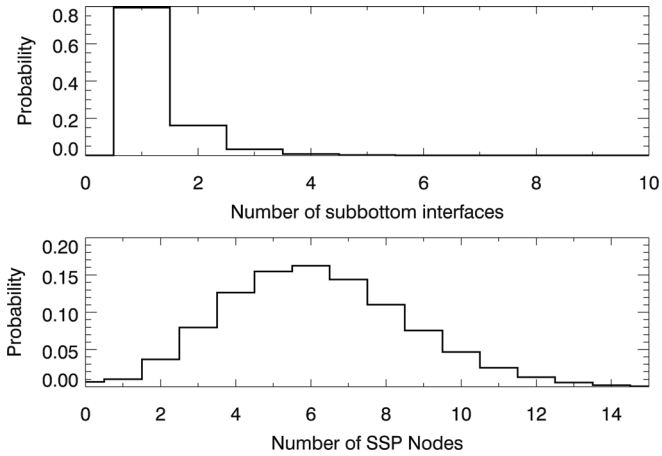

FIG. 8. Probability distributions of the number of (top) subbottom interfaces and (bottom) SSP nodes.

with an echosounder to be 41 m which is just outside this interval. The discrepancy may be due to the vessel's draft not being taken into account for the water depth measurement (unfortunately this is unknown) or poor echosounder calibration. Water depth measurements in subsequent years near the measurement site were around 43 m. Bathymetric effects are not likely to be significant since the bottom is so flat at the study location; tides are also not significant at this location.

The fit to the data is shown in Fig. 10. The relative arrival times from the mode-filtered spectrograms (picked data) are shown with × symbols and marginal densities of the relative arrival times, calculated from a random sample of 5000 models from the PPD, are shown in grey-scale. There is generally good agreement for all modes, frequencies, and pulses, with some indication of correlated errors. Figure 11 shows the error statistics for each mode and pulse in the same format as presented earlier. The residual standard deviations generally increase with mode number. This may be due to higher-order modes being more sensitive to finer scale environmental features that are less likely to be fully range independent. The AR process was required more often for higher-order modes and the AR coefficient a was generally positively correlated with the fraction of time the AR process was required. The standardized total residuals [Eq. (A4)] from the same sample of models used for Fig. 10 were examined (not shown here) to check the validity of the error model assumptions and found to be approximately Gaussian distributed with zero mean and unit standard deviation and had little autocorrelation between adjacent frequencies of each mode.

The marginal probability profiles for environmental parameters (Fig. 7) indicate the sensitivity in terms of the distribution widths; however, it can also be insightful and complementary to investigate environmental sensitivity from a forward-modeling perspective. Figure 12 shows the mode functions and transmission loss (TL) computed for the environmental model with highest likelihood from PPD samples collected in the inversion. This model has six SSP nodes, 42 m water depth, and one subbottom layer with thickness 14.5 m, sound speed 1630 m/s, and density 1.45 g/cm^3. The halfspace sound speed and density are 2384 m/s and 2.32 g/cm^3, respectively. The mode functions are shown for the lowest and highest frequencies from each picked mode. TL was computed assuming uniform sediment attenuation of 0.1 dB per wavelength and a point source at 2 m depth (the airgun depth). The water depth and subbottom interface are shown on the plots as horizontal lines. The mode functions show good subbottom penetration into the first ∼15 m of sediment, with lower frequencies penetrating deeper than higher frequencies. For the same frequency, higher-order modes penetrate deeper than lower-order modes (e.g., see

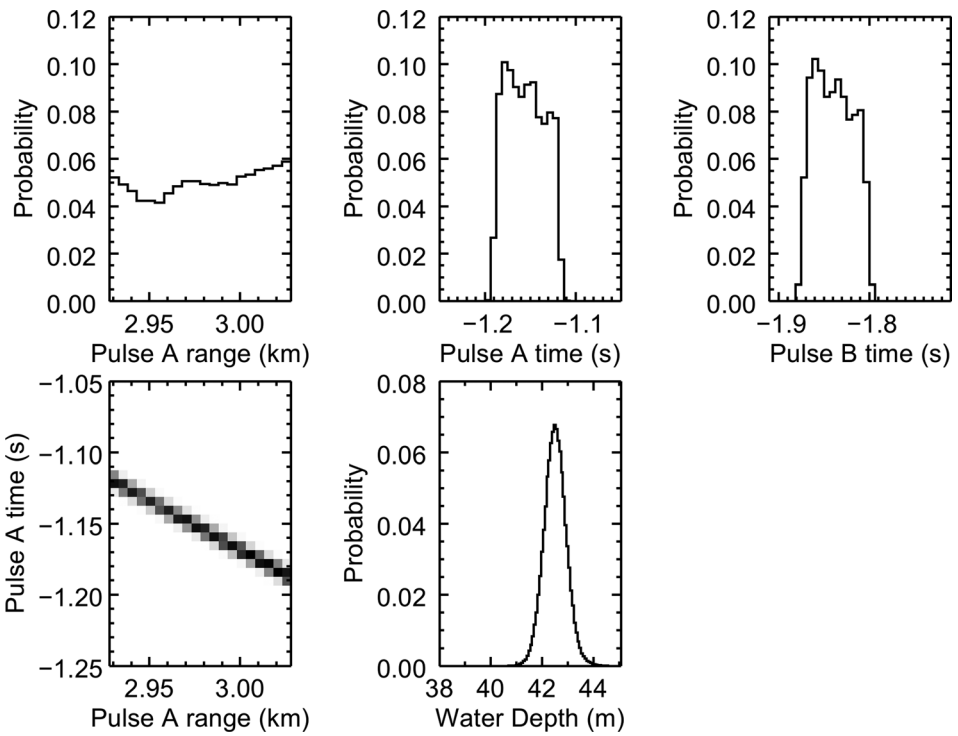

FIG. 9. Marginal probability densities for pulse range, time, and water depth for Chukchi Sea data. Pulse time axes are restricted within their prior distributions; all other axes ranges indicate prior bounds.

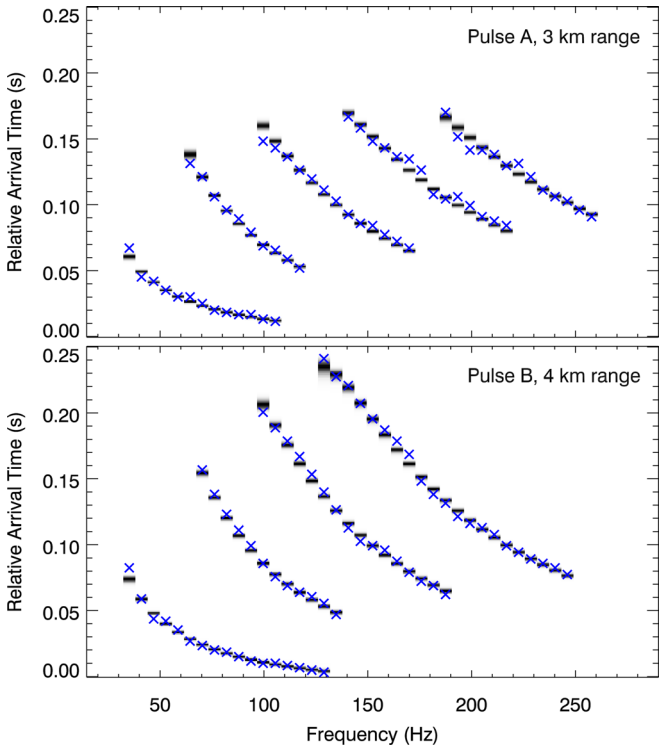

FIG. 10. (Color online) Mode relative arrival times for the two pulses calculated from a random sample of models from the PPD (grey-scale distributions) and the arrival times picked from the measured pulses (×).

the mode functions for the highest and lowest frequencies of modes 1 and 4, respectively, which are both for 128.9 Hz). Mode functions do not penetrate the halfspace well, which is consistent with the large uncertainties on estimated halfspace parameters. SSP resolution is more closely related to the mode function wavelength than the acoustic wavelength, i.e., higher-order modes are more important than higher frequencies for resolving finer-scale SSP features. It is also

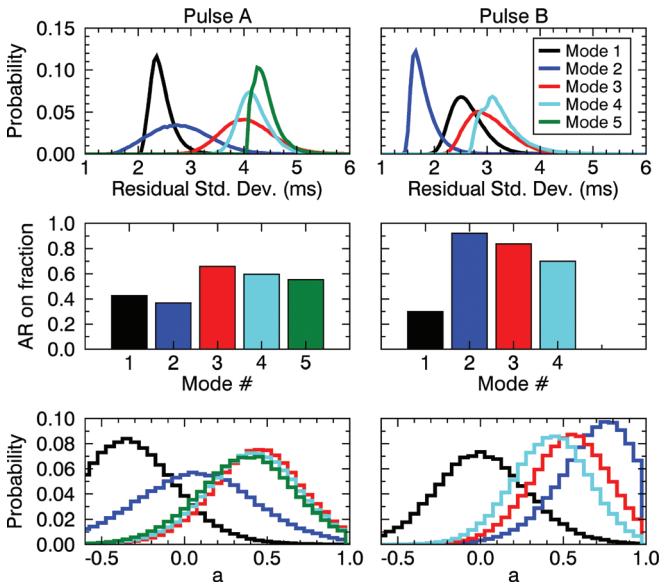

FIG. 11. Error statistics for modes in (left) pulse A and (right) pulse B. Residual standard deviations, fraction of time the AR process was required, and AR coefficient values are shown in the top, middle, and bottom panels, respectively.

interesting to note that near the seafloor is an ideal depth for making dispersion measurements as all of the mode functions have relatively high amplitudes at this depth (a hydrophone placed at a mode function null would be insensitive to that mode). The TL plots at 35.2, 99.6, and 252.0 Hz show decreasing seafloor penetration with frequency, but adequate penetration in the upper sediment layer to 4 km range for these frequencies.

A. Headwave inversion

To further corroborate the modal dispersion inversion results for this Chukchi Sea location, we performed an independent analysis of headwave arrival times to estimate the seafloor sound speed. Headwaves are longitudinal waves that travel along the seafloor or subbottom interfaces at the compressional-wave speed of the lower layer. They are excited by compressional waves incident on an interface at the critical angle, and as they propagate they generate upward-propagating compressional waves at the critical angle in the media above the interface.[27] These waves may arrive at a receiver before the direct waterborne acoustic wave if the source-receiver range is sufficiently large. Assuming uniform water and bottom sound speeds c_w and c_b, the arrival times for the waterborne wave and headwave are[27]

$$t_w = \sqrt{r^2 + (h_s - h_r)^2}/c_w \simeq r/c_w, \quad \text{for } r \gg h_s - h_r, \tag{4}$$

$$t_h = \frac{r}{c_b} + (h_s + h_r)\frac{\sqrt{c_b^2 - c_w^2}}{c_b c_w}, \tag{5}$$

where r is the source-receiver range, and h_s and h_r are the heights of the source and receiver above the seafloor, respectively. The arrival time difference between the waterborne path and headwave is

$$\Delta t \simeq r\left(\frac{1}{c_w} - \frac{1}{c_b}\right) - (h_s + h_r)\frac{\sqrt{c_b^2 - c_w^2}}{c_b c_w}. \tag{6}$$

This equation is linear with range and the slope of a Δt vs r plot can be used to calculate the seafloor sound speed if the water sound speed is known.

Low-frequency headwaves (∼140 Hz) were observed in the Chukchi Sea data before the direct-path arrival for pulses measured beyond approximately 250-m range. To determine accurate arrival times, pulse waveforms were stacked by manually time-aligning the direct-path arrivals. The low-frequency, low-amplitude headwaves were amplified by applying an automatic gain control (AGC) filter over the waveforms with a 0.02 s gate (Fig. 13, top). The headwave arrival times were picked from the peak arrival time for ranges between 320 and 490 m. A linear fit was calculated for the time difference between the direct and headwave arrivals (Fig. 13, bottom). Using Eq. (6) and an average water sound speed of 1443 m/s, the slope of the line and its uncertainty correspond to a seafloor sound speed of 1636 m/s and 95% credibility interval of [1629, 1643] m/s. On the

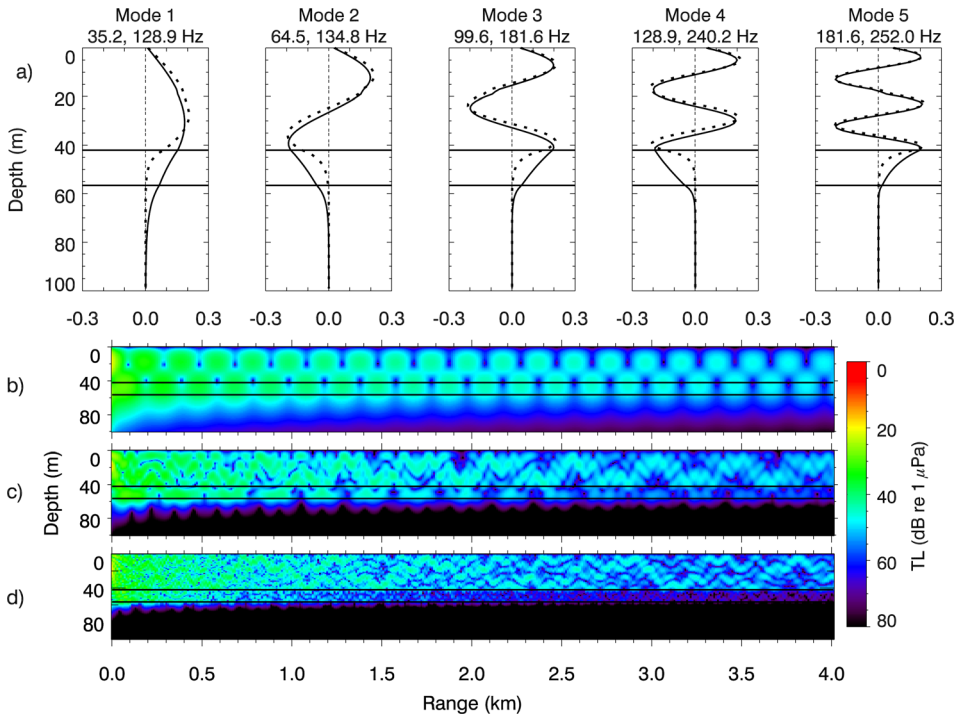

FIG. 12. (Color online) (a) Mode functions, and (b)–(d) TL for the maximum-likelihood environmental model. Solid horizontal lines indicate the water depth and subbottom layer interface depth. Mode functions for the lowest and highest frequencies picked from each mode are shown as solid and dashed curves, respectively (frequencies are indicated on each panel). TL is shown for 35.2, 99.6, and 252.0 Hz in (b)–(d), respectively.

basis of the modal dispersion inversion results, the most-probable subbottom sound speed from the PPD for the top 5 mbsf is 1633 m/s and the 95% credibility interval is [1612, 1647] m/s, which is in excellent agreement with the headwave results. Analysis of headwave arrival times can provide estimates of layer thicknesses and of sound speeds of deeper layers if headwaves off deeper layer interfaces can be detected in the acoustic data. Headwaves corresponding to the subbottom interface indicated in Fig. 7 at ∼10–20 mbsf were not discernable in the acoustic time series, so the thickness of the upper layer and sound speed of the halfspace in the modal inversion results could not be corroborated in this way.

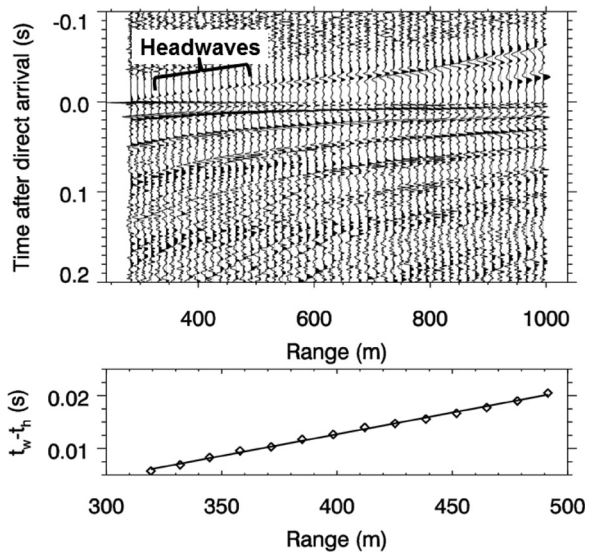

FIG. 13. Top plot shows stacked pulse waveforms aligned by the direct path arrival. Bottom plot shows time of arrival difference between the direct and headwave arrivals. AGC has been applied to the waveforms to show headwave arrivals.

VI. CONCLUSION

This paper presented trans-dimensional Bayesian inversion of modal dispersion data (both simulated and measured) at a single hydrophone. Mode arrival times were determined from time-frequency analysis of pulses after filtering individual modes using a warping procedure. The arrival times were then used in the inversion to estimate the water sound-speed profile, subbottom properties, and parameters of the survey which were not precisely known (pulse ranges and times). A trans-D framework was applied in three ways: for the water-column SSP, subbottom geoacoustic layering properties, and first-order auto-regressive error model.

The simulation study characterized the ability of the inversion to estimate environmental and experimental parameters. Limitations of the data processing method were shown through discrepancies in portions of the SSP. Dispersion data predicted using models from the PPD were shown to match the times estimated from synthetic time series via the data processing method. Autocorrelated errors between picked arrival times and the true times from theoretical dispersion curves are attributed to time-frequency data processing limitations which can be a major component of the errors.

Inversion results for the Chukchi Sea survey showed excellent agreement between the estimated SSP and the measured profile. The inversion resolved all significant features of the SSP, often requiring six or more sound-speed nodes to define the profile. The estimated geoacoustic profile showed less structure (two layers) but was well resolved for the shallowest layer. An independent headwave analysis for the seafloor sound speed agreed well with the modal-inversion estimates. The basement properties were less well resolved although the depth of the acoustic basement was well resolved. The ability to resolve SSP and seabed parameters via modal dispersion inversion agreed well

(qualitatively) with forward-modeling sensitivity analysis of the predicted mode functions and transmission loss. The estimated geoacoustic properties can be used to model sound propagation for noise-exposure estimation or marine-mammal localization at the measurement location.

Overall, modal dispersion data and the trans-D inversion approach are shown to be capable of estimating water SSP and subbottom sound speed and density profiles to about 10–20 m below seafloor with accuracy sufficient for many scientific purposes. The inversion results here from only two airgun array pulses provided useful profiles. The results are expected to be representative of the average properties over a 3–4 km path and are less susceptible to small scale variations that could influence spot measurements. Synchronized clocks for the source and receiver could remove the requirement to invert for absolute timing. Pulses could be produced by an autonomous system, so long term measurements could be possible.

ACKNOWLEDGMENTS

The authors thank Julien Bonnel of ENSTA Bretange for his code to perform the mode warping, and Michael Macrander and Louis Brzuzy of SEPCO for allowing us to publish results from their seismic survey. The authors thank the captain and crew of the *RV Mt. Mitchell* and Fugro staff for assistance in deploying and retrieving the OBH systems. The first author was supported by JASCO Applied Sciences and a Natural Sciences and Engineering Research Council (NSERC) of Canada Industrial Postgraduate Scholarship. The inversions were carried out on a computer cluster operated by the authors and funded by NSERC and ONR Ocean Acoustics.

APPENDIX: INVERSION FORMULATION

1. Trans-D Bayesian inversion

This section develops a trans-D Bayesian inversion for modal dispersion.[21,22] Let $\mathbf{d}$ be a random variable of N observed data and let $\mathbf{m}_k$ be a vector of M_k model parameters for a physical system of interest, where $k(\in \mathcal{K})$ indexes the form of the system representation. Green[12] showed that Bayes' rule can then be written

$$P(k,\mathbf{m}_k|\mathbf{d}) = \frac{P(k)P(\mathbf{m}_k|k)P(\mathbf{d}|k,\mathbf{m}_k)}{\sum_{k'\in\mathcal{K}}\int_{\mathcal{M}} P(k')P(\mathbf{m}'_{k'}|k')P(\mathbf{d}|k',\mathbf{m}'_{k'})d\mathbf{m}'_{k'}}. \tag{A1}$$

Equation (A1) represents a single hierarchical model of the physical system spanning several multi-dimensional subspaces. $P(k)$ is the prior distribution for k which indexes the number of subbottom interfaces, the number of nodes defining the water SSP, and the state of the AR(1) error model (described in Appendix Secs. 3, 4, and 5, respectively). $P(\mathbf{m}_k|k)$ is the prior distribution for the M_k model parameters. $P(\mathbf{d}|k,\mathbf{m}_k)$ is the conditional data error distribution; however, for fixed (measured) data $\mathbf{d}$, this probability is interpreted as the likelihood of the model parameters, $L(k,\mathbf{m}_k)$.

The trans-D posterior probability density (PPD) $P(k,\mathbf{m}_k|\mathbf{d})$ in Eq. (A1) can be approximated in a Markov-chain Monte Carlo (MCMC) simulation that can transition (jump) between system representations specified by k for models of dimension M_k. A reversible-jump MCMC (rjMCMC) algorithm[12] is used to sample the PPD while maintaining detailed balance for unbiased sampling.[28] Transitions from the current model $(k,\mathbf{m}_k)$ to a proposed model $(k',\mathbf{m}'_{k'})$ are accepted with probability given by the Metropolis-Hastings-Green criterion

$$\alpha = \min\left[1, \frac{P(k',\mathbf{m}'_{k'})}{P(k,\mathbf{m}_k)}\left(\frac{L(k',\mathbf{m}'_{k'})}{L(k,\mathbf{m}_k)}\right)^{1/T}\frac{Q(k,\mathbf{m}_k|k',\mathbf{m}'_{k'})}{Q(k',\mathbf{m}'_{k'}|k,\mathbf{m}_k)}|\mathbf{J}|\right], \tag{A2}$$

where $|\mathbf{J}|$ is the determinant of the Jacobian for the diffeomorphism from $(k,\mathbf{m}_k)$ to $(k',\mathbf{m}'_{k'})$ and T is the sampling temperature which can be considered unity here but is varied in the method of parallel tempering (described below). The rjMCMC algorithm used here is the birth-death scheme,[11] which has been used in several trans-D geoacoustic inversion studies.[15,21,29] For the trans-D geoacoustic profile, we implement this scheme by adding or removing subbottom interfaces which define homogeneous layers with sound speed and density. For a birth step, a new subbottom interface is inserted at a random depth selected from a uniform prior. The physical properties of the layer above the new interface are chosen randomly from the prior distribution. For a death step, an existing interface is randomly selected and removed. The physical parameters of the new thicker layer are chosen from the layer below the removed interface.

This birth/death scheme differs from that used in most trans-D geoacoustic inversion work. Previous studies have used symmetric proposal distributions centered around the current parameter values, so that high likelihood models will be proposed if the current model has high likelihood and the proposal distribution width is relatively small.[15] However, this can cause the proposal and prior ratios in Eq. (A2) to be small which decreases the acceptance probability. Dosso *et al.*[22] showed that birth acceptance rates could be much higher by proposing from the prior distribution compared to proposing close to the current model (the formulation is also simpler). We performed inversions using both schemes and found the acceptance rate was approximately four times higher when proposing from the prior than when using Gaussian proposals, resulting in faster PPD convergence.

In the water column, we implement the birth-death scheme by adding or removing SSP nodes which define a piecewise $1/c_w^2$ linear profile. Birth steps involve inserting a node with a depth and sound speed selected randomly from uniform prior distributions. For a death step, an existing node is randomly selected and removed. New parameter values are not needed for this step because the water SSP

effectively heals by joining the nodes above and below the removed node. The acceptance probability for the birth and death moves for either the water column or subbottom is given by Eq. (A2). These birth/death schemes ensure $|\mathbf{J}|$ is unity.[12]

Achieving efficient dimension jumps and complete sampling of potentially multi-modal structure within fixed-dimensional subspaces is a challenge in trans-D inversion.[22,29,30] One strategy is to use parallel tempering[29,31–34] which applies a sequence of interacting Markov chains that sample the PPD at different temperatures T [Eq. (A2)]. The acceptance probability α increases with T which allows more low-likelihood models to be accepted. Thus, higher-temperature chains sample the parameter space more freely, bridging potentially multimodal PPD structure or jumping dimension more readily. Lower temperature chains sample local PPD structure more efficiently. Chains with $T \neq 1$ do not provide unbiased sampling; however, the efficient exploration of the space provided by high temperature chains can be combined with unbiased $T = 1$ chains by allowing chains to probabilistically swap models according to the Metropolis-Hastings criterion: a swap of models between chains of temperatures T and T' is accepted with probability

$$p = \min\left[1, \left(\frac{L(k', \mathbf{m}'_{k'})}{L(k, \mathbf{m}_k)}\right)^{(1/T - 1/T')}\right]. \tag{A3}$$

Although the computational expense increases linearly with the number of parallel-tempering chains, the rate of PPD convergence may substantially outweigh this factor for suitably chosen temperatures.[31,32] The temperature spacing between chains is usually taken to be logarithmic with swaps allowed between arbitrary chain pairs.[32] For this paper, 10 rjMCMC chains were used with $T_i = 1.2^i$, $i = 0,\ldots, 9$.

There is no definitive test for convergence of Markov-chain sampling to the PPD[30] so it has been suggested that sampling should be conducted for some time after the PPD ceases to change significantly with new samples.[35] This can result in large sample populations which can take up large computer disk space and result in long post-processing times. Chain thinning[36] is used to reduce the correlation between samples and represent the PPD more efficiently, but it is difficult to know *a priori* how much to thin. The new method of fixed-length thinning[25] overcomes this by adaptively thinning samples based on a fixed number of desired PPD samples. New samples are probabilistically added to the PPD sample population by overwriting randomly selected existing samples while ensuring the probability of any two samples existing in the population is identical. The acceptance probability for the ith model in the chain is

$$\alpha_i = \begin{cases} 1, & i \leq N_{\text{tot}}, \\ \dfrac{\alpha_{i-1} N_{\text{tot}}}{\alpha_{i-1} + N_{\text{tot}}}, & i > N_{\text{tot}}, \end{cases}$$

where N_{tot} is the total number of samples in the desired population.

2. Likelihood

The likelihood function is dependent on the residual error statistics. These errors result from measurement, data-processing, and theory errors, the statistics of which are often unknown. The errors may have an autocorrelated component that we model using an AR(1) process.[15,37] The total data residuals for model $\mathbf{m}_k$ are given by

$$r_i = d_i - d_i(\mathbf{m}_k) - d_i(a), \tag{A4}$$

where

$$d_i(a) = a(d_{i-1} - d_{i-1}(\mathbf{m}_k)) \tag{A5}$$

is the AR(1) process and $\mathbf{d}(\mathbf{m}_k)$ are the predicted data. In this paper, the residual errors are assumed Gaussian distributed and the AR(1) coefficient a is restricted between -0.6 and 0.999. The validity of these error model assumptions are checked *a posteriori*. For N data with Gaussian-distributed errors the likelihood function is

$$L(k, \mathbf{m}_k) = \frac{1}{(2\pi)^{N/2} |\mathbf{C}_d|^{1/2}} \times \exp\left[-\frac{1}{2}\left(\mathbf{d} - \mathbf{d}(\mathbf{m}_k) - \mathbf{d}(a)\right)^T \mathbf{C}_d^{-1} \times \left(\mathbf{d} - \mathbf{d}(\mathbf{m}_k) - \mathbf{d}(a)\right)\right], \tag{A6}$$

where $\mathbf{C}_d$ is a diagonal data covariance matrix [given that error covariances are represented by the AR(1) process]. Errors are assumed independent between modes and between pulses, but potential correlation over frequency for a given mode m and pulse p is characterized by the AR(1) coefficient a_{mp}. Further, the error standard deviation (σ_{mp}) is assumed constant over frequency but potentially changes between pulses and modes. Let $\mathbf{d}_{mp}$ represent a vector of modal arrival times at N_{mp} frequencies. The likelihood function is the product

$$L(k, \mathbf{m}_k, \boldsymbol{\sigma}, \mathbf{a}) = \prod_{p=1}^{P_{\text{tot}}} \prod_{m=1}^{M_p} \frac{1}{\left(2\pi\sigma_{mp}^2\right)^{N_{mp}/2}} \times \exp\left[-\frac{|\mathbf{d}_{mp} - \mathbf{d}_{mp}(\mathbf{m}_k) - \mathbf{d}_{mp}(a_{mp})|^2}{2\sigma_{mp}^2}\right], \tag{A7}$$

where P_{tot} is the total number of pulses considered and M_p is the number of modes considered for pulse p. Setting $\partial L / \partial \sigma_{mp} = 0$ leads to a maximum-likelihood estimate for σ_{mp}:

$$\hat{\sigma}_{mp}(\mathbf{m}_k) = \left[|\mathbf{d}_{mp} - \mathbf{d}_{mp}(\mathbf{m}_k) - \mathbf{d}_{mp}(a_{mp})|^2 / N_{mp}\right]^{1/2}. \tag{A8}$$

Substituting Eq. (A8) into Eq. (A7) and neglecting multiplicative constants gives

$$L(k, \mathbf{m}_k, \mathbf{a}) = \exp\left[-\sum_{p=1}^{P_{\text{tot}}} \sum_{m=1}^{M_p} N_{mp} \times \log_e |\mathbf{d}_{mp} - \mathbf{d}_{mp}(\mathbf{m}_k) - \mathbf{d}_{mp}(a_{mp})|\right], \tag{A9}$$

which provides an efficient treatment of unknown σ_{mp} without explicitly sampling additional parameters.[29]

3. Prior and proposal ratios—Geoacoustics

Markov-chain moves for the geoacoustic parameters that do not change model dimension (i.e., number of subbottom layers) have unity prior and proposal ratios in Eq. (A2) because we use a uniform prior $P(\mathbf{m}_k)$ and a symmetric (Gaussian) proposal distribution centered at the current parameter value. For moves that change dimension, the prior and proposal ratios are not unity. The prior distribution can be written

$$P(k,\mathbf{m}_k) = P(k)P(\mathbf{m}_k|k) = P(k)P(\mathbf{z}|k)P(\mathbf{c}_b,\boldsymbol{\rho}|k), \quad \text{(A10)}$$

where $\mathbf{z}$ represents the set of subbottom interface depths, $\mathbf{c}_b$ and $\boldsymbol{\rho}$ represent layer sound speeds and densities, and k is taken here to represent the number of subbottom interfaces. The prior distribution for k is uniform from the assigned minimum to the maximum number of interfaces (0 and 10 for this paper, respectively). The prior distribution for the depth partition $\mathbf{z}$ is a Dirichlet distribution given by[22,25]

$$P(\mathbf{z}|k) = k! z_b^{-k}, \quad \text{(A11)}$$

where z_b is a fixed maximum interface depth (50 m for this paper), below which the data are insensitive and structure cannot be resolved, and the prior distribution for z_i is uniform over $[0, z_b]$. The subbottom sound speed c_b and density ρ are bound by a joint prior distribution representing an empirical relationship based on a compilation of sediment samples to constrain models to physical speed and density combinations.[23,24]

The proposal ratio for moves that jump dimension can be broken down into

$$\frac{Q(k,\mathbf{m}_k|k',\mathbf{m}'_{k'})}{Q(k',\mathbf{m}'_{k'}|k,\mathbf{m}_k)} = \frac{Q(k|k',\mathbf{m}'_{k'})}{Q(k'|k,\mathbf{m}_k)}\frac{Q(\mathbf{z}|k',\mathbf{m}'_{k'})}{Q(\mathbf{z}'|k,\mathbf{m}_k)} \times \frac{Q(\mathbf{c}_b,\boldsymbol{\rho}|k',\mathbf{m}'_{k'})}{Q(\mathbf{c}'_b,\boldsymbol{\rho}'|k,\mathbf{m}_k)}. \quad \text{(A12)}$$

The proposal ratio for k cancels because $Q(k)$ is symmetric. Using the depth partition prior in Eq. (A11) and drawing subbottom sound speed and density in birth steps from the joint prior results in the proposal ratio cancelling the prior ratio in the acceptance probability equation, leaving

$$\alpha = \min\left[1, \frac{L(k',\mathbf{m}'_{k'})}{L(k,\mathbf{m}_k)}\right]. \quad \text{(A13)}$$

4. Prior and proposal ratios—Sound-speed profile

The water SSP parameterization in this paper consists of sound speeds defined at the surface and seafloor, and sound speeds and depths defined at an unknown number of nodes within the water column (0–15 nodes are allowed here). A uniform prior is used for the number of nodes and for all speeds and depths, and proposals for parameter perturbations are based on a symmetric (Gaussian) distribution centered at the current parameter value. This ensures that most terms of the prior and proposal ratios in Eq. (A2) cancel; however, in contrast to the geoacoustic layer-stack model, the prior distribution for the SSP node-depth partition does not generally cancel.

Markov-chain moves that do not change the dimension of the SSP have unity prior and proposal ratios, except for moves that change the water depth. The prior distribution for the node depth partition $P(\mathbf{z}|k)$ is of the same form as in Eq. (A11) except that z_b is now the water depth and k is the number of water-column nodes. It is straightforward to show that the acceptance probability for birth, death, and perturbation moves for the SSP becomes

$$\alpha = \min\left[1, \left(\frac{z_b}{z'_b}\right)^k \frac{L(k',\mathbf{m}'_{k'})}{L(k,\mathbf{m}_k)}\right], \quad \text{(A14)}$$

which reduces to the likelihood ratio for moves where z_b remains constant.

5. Trans-D AR model

A trans-D algorithm is also applied to the residual error model[15] where index k takes one of two values: $k=0$ indicates an error model without an auto-regressive component and $k=1$ indicates an AR(1) process with coefficient $a \in (-0.6, 0.999)$. Let a_k represent the AR(1) parameter for a particular mode and pulse. Three moves are possible and are chosen with equal probability: birth of the AR(1) parameter, death of the AR(1) parameter, or a perturbation to a_1. A uniform prior distribution is used for birth moves and a symmetric (Gaussian) distribution is used for perturbation moves. The resulting acceptance probability is

$$\alpha = \min\left[1, \gamma\frac{L(a')}{L(a)}\right], \quad \text{(A15)}$$

where γ is 0.5, 2, and 1 for birth, death, and perturbation moves, respectively.[15]

[1] F. B. Jensen, W. A. Kuperman, M. B. Porter, and H. Schmidt, *Computational Ocean Acoustics, Series in Modern Acoustic and Signal Processing* (AIP Press, New York, 1993), pp. 271–333.
[2] J. Bonnel and N. R. Chapman, "Geoacoustic inversion in a dispersive waveguide using warping operators," J. Acoust. Soc. Am. **130**, EL101–EL107 (2011).
[3] J. Zeng, N. R. Chapman, and J. Bonnel, "Inversion of seabed attenuation using time-warping of close range data," J. Acoust. Soc. Am. **134**, EL394–EL399 (2013).
[4] J. Bonnel, C. Gervaise, B. Nicolas, and J. I. Mars, "Single-receiver geoacoustic inversion using modal reversal," J. Acoust. Soc. Am. **131**, 119–128 (2012).
[5] J. Bonnel, B. Nicolas, J. I. Mars, and S. C. Walker, "Estimation of modal group velocities with a single receiver for geoacoustic inversion in shallow water," J. Acoust. Soc. Am. **128**, 719–727 (2010).
[6] J. Bonnel, S. E. Dosso, and N. R. Chapman, "Bayesian geoacoustic inversion of single hydrophone light bulb data using warping dispersion analysis," J. Acoust. Soc. Am. **134**, 120–130 (2013).
[7] G. Potty, J. Miller, P. Wilson, J. Lynch, and A. Newhall, "Geoacoustic inversion using combustive sound source signals," J. Acoust. Soc. Am. **124**, EL146–EL150 (2008).

[8]G. Potty, J. Miller, J. Lynch, and K. Smith, "Tomographic inversion for sediment parameters in shallow water," J. Acoust. Soc. Am. **108**, 973–986 (2000).
[9]G. Potty, J. Miller, and J. Lynch, "Inversion for sediment geoacoustic properties at the New England Bight," J. Acoust. Soc. Am. **114**, 1874–1887 (2003).
[10]G. Potty, J. Miller, P. Dahl, and C. Lazauski, "Geoacoustic inversion results from the ASIAEX East China Sea Experiment," IEEE J. Ocean. Eng. **29**, 1000–1010 (2004).
[11]C. Geyer and J. Moller, "Simulation procedures and likelihood inference for spatial point processes," Scand. J. Stat. **21**, 359–373 (1994).
[12]P. J. Green, "Reversible jump Markov chain Monte Carlo computation and Bayesian model determination," Biometrika **82**, 711–732 (1995).
[13]A. Malinverno, "Parsimonious Bayesian Markov chain Monte Carlo inversion in a non-linear geophysical problem," Geophys. J. Int. **151**, 675–688 (2002).
[14]M. Sambridge, K. Gallagher, A. Jackson, and P. Rickwood, "Trans-dimensional inverse problems, model comparison and the evidence," Geophys. J. Int. **167**, 528–542 (2006).
[15]G. Steininger, J. Dettmer, S. E. Dosso, and C. W. Holland, "Trans-dimensional joint inversion of seabed scattering and reflection data," J. Acoust. Soc. Am. **133**, 1347–1357 (2013).
[16]C. M. Reiser, D. W. Funk, R. Rodrigues, and D. Hannay, "Marine mammal monitoring and mitigation during open water seismic exploration by Shell Offshore, Inc. in the Alaskan Chukchi Sea, July-October 2009: 90-day report," Technical Report P1112-1, LGL Alaska Research Associates Inc. and JASCO Research Ltd. (2010), available at http://www.nmfs.noaa.gov/pr/pdfs/permits/shell_openwater_report2009.pdf.
[17]H. M. Feder, A. S. Naidu, S. C. Jewett, J. M. Hameedi, W. R. Johnson, and T. E. Whitledge, "The northeastern Chukchi Sea: Benthos-environmental interactions," Mar. Ecol. Prog. Ser. **111**, 171–190 (1994).
[18]A. L. Blanchard, C. L. Parris, A. L. Knowlton, and N. R. Wade, "Benthic ecology of the northeastern Chukchi Sea. Part I. Environmental characteristics and macrofaunal community structure, 2008–2010," Cont. Shelf Res. **67**, 52–66 (2013).
[19]E. K. Westwood, C. T. Tindle, and N. R. Chapman, "A normal mode model for acousto-elastic ocean environments," J. Acoust. Soc. Am. **100**, 3631–3645 (1996).
[20]G. Le Touzé, B. Nicolas, J. I. Mars, and J. Lacoume, "Matched representations and filters for guided waves," IEEE Trans. Signal Process. **57**, 1783–1795 (2009).
[21]J. Dettmer, S. E. Dosso, and C. W. Holland, "Trans-dimensional geoacoustic inversion," J. Acoust. Soc. Am. **128**, 3393–3405 (2010).
[22]S. E. Dosso, J. Dettmer, G. Steininger, and C. Holland, "Efficient trans-dimensional Bayesian inversion for geoacoustic profile estimation," Inverse Problems **30**, 114018 (2014).
[23]D. R. Jackson and M. D. Richardson, *High-Frequency Seafloor Acoustics*, 1st ed. (Springer, New York, 2007), pp. 178–200.
[24]J. E. Quijano, S. E. Dosso, J. Dettmer, L. M. Zurk, M. Siderius, and C. Harrison, "Bayesian geoacoustic inversion using wind-driven ambient noise," J. Acoust. Soc. Am. **131**, 2658–2667 (2012).
[25]G. Steininger, "Determination of seabed acoustic scattering properties by trans-dimensional Bayesian inversion," Ph.D. thesis, School of Earth and Ocean Sciences, University of Victoria, Victoria, BC, Canada (2013).
[26]R. A. Woodgate, K. Aagaard, and T. J. Weingartner, "A year in the physical oceanography of the Chukchi Sea: Moored measurements from autumn 1990–1991," Deep Sea Res. II **52**, 3116–3149 (2005).
[27]W. M. Telford, L. P. Geldart, R. E. Sheriff, and D. A. Keys, *Applied Geophysics* (Cambridge University Press, Cambridge, UK, 1976), pp. 218–441.
[28]D. J. C. MacKay, *Information Theory, Inference, and Learning Algorithms* (Cambridge University Press, Cambridge, UK, 2003), pp. 343–386.
[29]J. Dettmer and S. E. Dosso, "Trans-dimensional matched-field geoacoustic inversion with hierarchical error models and interacting Markov chains," J. Acoust. Soc. Am. **132**, 2239–2250 (2012).
[30]C. J. Geyer, *Introduction to Markov Chain Monte Carlo* (Springer, New York, 2011), pp. 3–47.
[31]S. E. Dosso, C. W. Holland, and M. Sambridge, "Parallel tempering for strongly nonlinear geoacoustic inversion," J. Acoust. Soc. Am. **132**, 3030–3040 (2012).
[32]M. Sambridge, "A parallel tempering algorithm for probabilistic sampling and multimodal optimization," Geophys. J. Int. **196**, 357–374 (2014).
[33]D. J. Earl and M. W. Deem, "Parallel tempering: Theory, applications, and new perspectives," Phys. Chem. Chem. Phys. **7**, 3910–3916 (2005).
[34]A. Jasra, D. A. Stephens, and C. Holmes, "Population-based reversible jump Markov chain Monte Carlo," Biometrika **94**, 787–807 (2007).
[35]A. Jasra, D. A. Stephens, and C. C. Holmes, "On population-based simulation for static inference," Stat. Comp. **17**, 263–279 (2007).
[36]A. F. M. Smith, "Bayesian computational methods," Philos. Trans. R. Soc. Lond. **337**, 369–386 (1991).
[37]J. Dettmer, S. Molnar, G. A. M. W. Steininger, S. E. Dosso, and J. F. Cassidy, "Trans-dimensional inversion of microtremor array dispersion data with hierarchical autoregressive error models," Geophys. J. Int. **188**, 719–734 (2012).